The effect of mixing order of Si and Al sources on the inner architecture and catalytic performance of ZSM-5 zeolites

Yanfeng Shen, Shang Zhang, Zhengxing Qin, Antoine Beuque, Ludovic Pinard, Shunsuke Asahina, Natsuko Asano, Ruizhe Zhang, Jiaqi Zhao, Yuhao Fan, et al.

The effect of mixing order of Si and Al sources on the inner architecture and catalytic performance of ZSM-5 zeolites

Yanfeng Shen[1], Shang Zhang[2,3], Zhengxing Qin[1], Antoine Beuque[4], Ludovic Pinard[5], Shunsuke Asahina[6], Natsuko Asano[6], Ruizhe Zhang[1], Jiaqi Zhao[1], Yuhao Fan[1], Xinmei Liu[1], Zifeng Yan[1], Svetlana Mintova[1,5*]*

[1]State Key Laboratory of Heavy Oil Processing, College of Chemical Engineering, China University of Petroleum (East China), No. 66, West Changjiang Road, Huangdao District, Qingdao, China, 266580

[2]Petrochemical Research Institute, PetroChina Company Limited, Beijing 100195, P. R. China

[3]West Pacific Petrochemical Company LTD, Dalian, China, 116000

[4]Université de Poitiers, UFR SFA, IC2MP, UMR 7285, Bât B27, 4 rue Michel Brunet, TSA 51106, 86073 Poitiers Cedex 9, France

[5]Laboratoire Catalyse et Spectrochimie, Normandie University, ENSICAEN, UNICAEN, CNRS, 6 Bd Marchal Juin, Caen, France, 14000

[6]SEM Application Team JEOL Ltd. 3-1-2 Musashino, Akishima, Tokyo, Japan, 196-8558

Corresponding Author: Zhengxing Qin* (zhengxing.qin@upc.edu.cn); Svetlana Mintova* (svetlana.mintova@ensicaen.fr)

ABSTRACT

The performance of zeolites in catalysis and adsorption is closely related to their inner architecture beneath the crystals surface, which however remains less studied due to characterization limitations. Here we report the synthesis of two ZSM-5 zeolite samples by changing only the order of mixing of Si and Al sources resulting not only in morphological differences of the zeolite crystals but most importantly in defined distinction in their inner architecture. The spatial Si and Al distributions and structural properties of the ZSM-5 zeolite crystals were characterized by high-resolution microscopy under chemically unbiased defect-selective NH_4F etching. The Al-zoning and structural features in the ZSM-5 zeolite crystals were explained by the biased nucleation in the Si-rich aluminosilicate amorphous precursor followed by multi-stage crystal growth in a heterogeneous feedstock. This observation was associated with the different solubility and reactivity of the microscopic aluminosilicate domains with various Si/Al ratios in the amorphous precursors. The zeolites with diverse structural properties showed a high cracking activity in n-hexane cracking reaction and different activity, stability and product selectivity in the ethylene dehydroaromatization reaction. The comprehensive understanding of the zeolite synthesis history and their performance in the EDA reaction revealed the chemical mixing dependent synthesis–structure–performance correlation of the zeolite catalyst.

KEYWORDS: Zeolites; Al-zoning; Chemical mixing order; Crystallization mechanism; Inner architecture; Ethylene dehydroaromatization

1. Introduction

Zeolites are important solid catalysts with wide applications in multiple reactions due to their open framework structures with outstanding (hydro)thermal stability, adjustable acidity, and unique shape selectivity [1-4]. In practice, however, activity, selectivity, and deactivation by coking are some other unavoidable issues that need to be addressed independently. These inevitable consequences essentially depend on the synthesis pathway of the zeolite catalysts. In order to improve the properties of zeolite catalysts, the main focus was on the optimization of some readily measurable properties such as the crystallization rate [5], the crystal size and morphology [6], the acid type and concentration [7-9], the secondary porosity [10-13], etc. In this regard, many variables have been identified as important factors impacting zeolite crystallization. For example, both the synthesis temperature and crystallization time have important roles due to the metastable nature of zeolites [14, 15]. Besides, the type and source of raw materials (purities, reactivity), the composition of precursor mixtures, the use of different organic and/or inorganic structure-directing agents, order of mixing of chemicals, agitation, and aging all have a significant impact on the properties of the final zeolite [16, 17]. In recent years, the trajectory of zeolite crystal design has shifted from the macroscopic to the microscopic level [18]. This has been synchronized with the knowledge acquired on the specific position of framework T atoms such as (Al, Ti, etc.) that can have a vital impact on the zeolite properties [19]. As a result, one of the main interests is the development of synthetic methods towards the positioning of framework active sites in zeolites by pre-design strategy [20]. In contrast, the inner

architecture beneath the zeolite surface remains less explored in zeolite research. The inner architecture describes the structural characteristics of zeolite domains hidden beneath the outer surface of zeolite crystals. In most cases, the dimension used to describe such an inner architecture is within the 2-50 nm scale. For example, the presence of zeolite subunits [21, 22], and the presence of different misaligned zeolite domains in the crystals have been reported [23]. Additionally, the presence of framework defects including silanol groups and Brønsted acid sites (BAS) in the zeolites with Al spatial location have been discussed [18, 21, 24-32]. Since most of the reaction events happen inside the volume of zeolite crystals. It is not surprising that an interruption of the micropore coherence or the presence of crystal imperfection (silanols) can impact the diffusion, adsorption, and conversion in zeolites. Likewise, heterogeneous ZSM-5 nanocrystals with core-shell structures were synthesized, and the impact of the element zoning phenomenon on their catalytic performance was also investigated [33-36]. Although it may seem obvious and this can always be roughly attributed to some ambiguous "structure-properties" dependence, a comprehensive investigation of the inside architecture of zeolite crystals and a comprehensive understanding of the crystal growth mechanism remain challenging due to the lack of powerful and convincing characterization approaches [21, 31, 36-].

In a recent study [44], we investigated the inner architecture and heterogeneity of pseudo-single ZSM-5 zeolite crystals. It was found that the zeolite crystals showed characteristic defect (structural imperfection)-zoning and Al-zoning as a result of a three-stage crystal growth process involving (i) the nucleation resulting in the Si-rich

innermost core formation, (ii) the fast aggregate growth leading to defect-rich zones, and (iii) the layer-by-layer growth shaping the final morphology of the zeolite crystals. A clear correlation between Al zoning and the spatial distribution of C and Na for the ZSM-5 crystals in this particular system was founded.

The objective of the present study is to investigate the effect of mixing order of silica and alumina sources on the inner architecture of ZSM-5 zeolite crystals. Several studies have pointed out to the effect of mixing order of raw materials on the topology of the final products [45], the crystallization rate [5, 46-49], or the degree of incorporation and distribution of Al in the framework [24, 50]. However, there are still relatively few systematic studies focusing on the effect of chemicals' mixing order on the arrangement of elements and defects in the zeolite crystals [51-53]. In the present work, two ZSM-5 zeolites were prepared under identical experimental conditions following the same synthetic recipe except that the mixing order of Al- and Si- sources (Z_{Al} and Z_{Si} samples) were exchanged. The different structural properties, including the Al-zoning and defect-zoning phenomenon, inside of the two zeolite crystals have been revealed. And the explanations for the formation of zeolites with diverse properties have also been provided. Furthermore, the ethylene dehydroaromatization (EDA) reaction was used performed to highlight the importance of the zeolite crystals' inner structural properties.

2. Experimental

2.1 Zeolite synthesis

2.1.1 Synthesis of Z_{Al} zeolite samples by adding Al source first to the precursor mixture.

For the synthesis, 20.3 g of the tetrapropyl ammonium hydroxide (TPAOH, Chemical Reagent Co., Ltd., 25.0% wt.% sol.) and 2.5 g of the sodium hydroxide (NaOH, Chemical Reagent Co., Ltd., 96.0 wt.%) were dissolved in 450 g deionized water followed by the addition of 3.75 g $Al(NO_3)_3 \cdot 9H_2O$ (Sinopharm Chemical Reagent Co., Ltd., 99.0% wt.%) under stirring at room temperature. After the complete dissolution of $Al(NO_3)_3 \cdot 9H_2O$, 52 g tetraethyl orthosilicate (TEOS, Sinopharm Chemical Reagent Co., Ltd., AR) was added, and the obtained mixture was kept in a closed PP (polypropylene) bottle overnight under stirring at room temperature (RT) for the hydrolysis of the TEOS. The final precursor transparent gel with a molar ratio of 1.0 SiO_2: 0.02 Al_2O_3: 0.25 NaOH: 0.1 TPAOH: 100 H_2O, was transferred into a Teflon-lined autoclave and subjected to hydrothermal (HT) treatment at 443 K for 24 h. The final product Z_{Al} was recovered by filtration and washed thoroughly with deionized water, and dried at 373 K in oven overnight.

2.1.2 Synthesis of Z_{Si} zeolite samples by adding Si source first to the precursor mixture.

For the preparation of the Z_{Si} zeolite sample, TEOS was firstly added to the solution prepared by dissolving 2.5 g NaOH and 20.3 g TPAOH into 450 g deionized water. The mixture was kept stirring in a closed PP bottle overnight at RT until the thorough hydrolysis of the TEOS. Then the Al source was added and the final precursor

mixture was kept under stirring for 1 h. The crystallization and purification processes were carried in the same manner as for the Z_{Al} samples described above.

Intermediate products were collected from both precursor mixtures subjected to less than 24 h HT treatment. The solids were collected by centrifugation and washed with deionized water thoroughly. The obtained intermediate solids were denoted as Z_{Al}-x or Z_{Si}-x, where the suffix x represents the time of HT treatment. To remove the organic template, the as-prepared zeolite samples were calcined at 823 K for 12 hours under statistic air conditions with a ramp of 2 K/min. The synthesis of the Z_{Si} was repeated for 3 times, and the samples obtained from the second and the third batches were named Z_{Si}-B2 and Z_{Si}-B3, respectively.

2.1.3 Synthesis of $Z_{Si}^{'}$ zeolite samples with an extended aging of the precursor.

For the synthesis of sample $Z_{Si}^{'}$, the same synthesis procedures as for the Z_{Si} was used (**Section 2.1.2**). The only difference included after the addition of the Al source was that the final precursor mixture was kept under stirring for 12 or 60 h instead of 1h before it was transferred to the autoclaves. The final zeolite products were named as $Z_{Si}^{'}$-12A and $Z_{Si}^{'}$-60A, respectively.

2.2 Post-synthesis treatment of Z_{Al} and Z_{Si} zeolite samples by NH_4F etching

The parent ZSM-5 zeolite samples (Z_{Al} and Z_{Si}) were treated with NH_4F solution following the method described in our previous paper [44]. 4 g zeolite samples were added into 120 g NH_4F solution (40 wt. %) and kept stirring under 323 K for 4 hours. The treated samples were recovered by filtration, washed with deionized water and

dried at 373 K overnight. The products obtained after the post-synthesis treatment of samples Z_{Al} and Z_{Si} were denoted as Z_{Al}-AF and Z_{Si}-AF, respectively.

2.3 Characterization

The XRD patterns of the zeolite samples were collected on a Bruker D8 Advance instrument with Cu Kα radiation. The particle size distribution in the zeolite precursor gels was measured with dynamic light scattering (DLS, Malvern Nano ZS).

The morphology of precursor gel particles and zeolite crystals was characterized by a low-voltage-high-resolution field emission scanning electron microscope (SEM, JSM-7900F, JEOL). The cross-sections of the zeolite samples were prepared with an ion beam cross-section polisher (IB-19510CP, JEOL). The SEM-EDX mapping was recorded with an Oxford EDS detector (EDS 170 mm x 2) following the procedure developed by Asahina et al. [54]. Before the measurement, a 3 nm Os layer was sprayed on the surface of the zeolite cross section to improve the conductivity. The TEM images were taken on a transmission electron microscope (TEM, JEM-2100, JEOL) with an accelerate voltage of 200 kV.

The bulk chemical composition of zeolites was determined by XRF on an AXIOS-Petro X (PANalytical B.V.). The surface Si/Al of zeolite crystals was measured by X-ray photoelectron spectroscopy (XPS) using a PHI 500 spectrometer equipped with an Al Kα radiation. Both the ^{29}Si and ^{27}Al MAS spectra of as-synthesized zeolite samples were collected without calcination and ion exchange treatment. The ^{29}Si MAS NMR spectra were recorded on a Bruker Advance 400

spectrometer using a relaxation delay of 3 s. The ^{27}Al MAS NMR spectra were collected on a Bruker Advance 500 spectrometer.

The H^+-form of the zeolite samples were subjected to FTIR analysis. To remove the organic template, the as-synthesized zeolites were calcined at 823 K for 12 hours with a ramp of 2 K/min. The calcined zeolites were then subjected to NH_4^+ exchange. And the procedure was repeated three times before drying overnight at 373 K. Finally, the H^+-form zeolite samples were prepared after removing the NH_4^+ under heating at 823 K for 4 h). The IR spectra of the zeolite samples were obtained on the Nicolet Magna 550-FT-IR spectrometer at 2 cm^{-1} optical resolution. Prior to the measurement, the H^+-form zeolite samples were pressed into a ca. 18 mg self-supporting discs and pretreated at 823 K in a vacuum of 10^{-6} Torr for 5 h. The pyridine or collidine was used as a probe molecule to determine the acid sites of zeolite samples. The amount of the Brønsted and Lewis sites was calculated by integrating the peaks at 1545 cm^{-1} and 1454 cm^{-1} of the FTIR spectra recorded under adsorption of pyridine, respectively. The surface acidity of the zeolite crystals was using the collidine probe molecule. The IR spectra of the samples were collected after the collidine desorption at 423k. The calculation was carried out based on the absorbance peak between ca. 1620 and 1660 cm^{-1} using an extinction coefficient ε (collidine) = 10.1 cm.μmol^{-1}. The porosity of zeolites was probed using an Autosorb iQ3 (Qutantachrome) either by Argon at 87 K for the intermediate products or N_2 at 77 K for the well-crystalline zeolites. The specific surface area and micropore volume of the samples were calculated with the BET (Brunauer-Emmett-Teller) and t-plot method, respectively.

2.4 Evaluation of zeolite samples in n-hexane cracking reaction

The catalytic test of zeolite samples in n-hexane cracking reaction was carried out using a throughput four-parallel fixed-bed reactors unit. Different amounts of the same catalyst with a particle size of 0.2-0.5 mm were put in each reactor (20, 40, 60 and 80 mg) and pre-treated at 813 K under nitrogen flow for 12 h. Diluted n-hexane (99.99 % pure from Sigma Aldrich) in nitrogen flow was then injected in the reactors at 813 K with a molar ratio of 11 ($P_{N2}/P_{n\text{-}hexane} = 11$). Catalyst' activity is measured by estimating the conversion at different values of the weight hour space velocity (WHSV). Reaction products were analyzed on-line by GC450 gas Chromatography equipped with a Cp-Al_2O_3/Na_2SO_4 capillary column (50 m, 10 µm) coupled with a FID detector. The turn over frequency (TOF, h^{-1}), was calculated as followed: $TOF = \frac{A}{[B_{py}] \times M_{n-hexane}}$, with A: $g_{n\text{-}hexane}/h/g_{catalyst}$, $[B_{py}]$: the acidity was determined by pyridine adsorption followed by IR ($\mu mol/g_{catalyst}$), and the $M_{n-hexane}$ is the molar weight of the n-hexane (g/mol).

2.5 Evaluation of zeolite samples in ethylene dehydroaromatization reaction.

The catalytic performance of the zeolite samples was tested in ethylene dehydroaromatization reaction in a fixed-bed continuous flow quartz reactor under atmospheric pressure at 973 K. Ethylene (Air Liquid, > 99 %) was diluted in a nitrogen flow with a partial pressure of 0.005 MPa. Under standard conditions, the ethylene gas weight hourly space velocity (WHSV, g of injected C_2H_4 per hour and per g of catalyst) was 14 h^{-1}, and the gas hourly space velocity was 240 000 ml g_{cat}^{-1}

h^{-1}. Prior to the catalytic test, the zeolite samples were compacted with a pressure of 3 tons, crushed and sieved to obtain a homogeneous mash of 0.2 - 0.4 mm.

Firstly, the zeolite samples were pre-treated under nitrogen flow (100 mL min^{-1}) for one hour at 973 K with a heating rate of 10 K min^{-1}. Then the gas feed was switched to the gas mixture of ethylene diluted in N_2 (5% C_2H_4/N_2). The gaseous products and hydrogen were analyzed on-line by a Varian CP-3800 gas chromatograph equipped with an FID detector connected to a fused silica J&W GS-Gaspro capillary column (60 m x 0.32 mm x 4 μm) and a TCD connected to a J&W PoraPLOT Q-HT capillary column (25 m x 0.53 mm x 20 μm).

2.6 Characterization of spent zeolite catalysts

After 10 hours of reaction, the feed gas was stopped and switched to a nitrogen flow while the reactor was quenched under an external airflow. The amount of coke in the spent zeolite catalysts was quantified by thermogravimetric analysis using a SDT Q600 TA thermogravimetric analyzer. The spent catalyst was kept for 30 min in a dry air stream under a flow rate of 100 mL min^{-1} and then heated with a rate of 10 K min^{-1} till 1173 K. Once the final temperature was reached, the temperature was kept for 10 min followed by cooling.

3. Results and discussion

3.1 Similarities of Z_{Al} and Z_{Si} zeolite samples

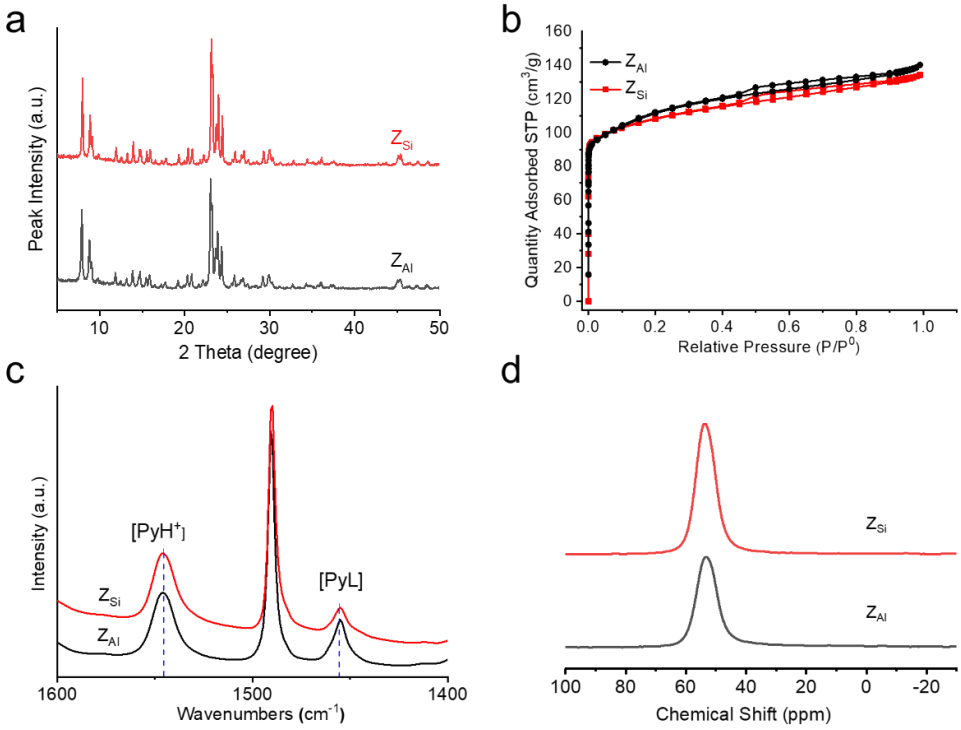

Figure 1. Structural analysis of Z_{Si} and Z_{Al} zeolite samples: (a) XRD patterns, (b) N_2 physisorption isotherms at 77 K, (c) FTIR spectra of the acidity region after pyridine desorption at 423 K, and (d) ^{27}Al NMR spectra of the as-synthesized Z_{Si} and Z_{Al} samples.

The alternation of the mixing sequence of Al and Si sources did not change the macroscopic properties of the synthesized zeolite samples. Both precursor mixtures resulted in highly crystalline and phase-pure ZSM-5 zeolites (Figure 1a). The shape of the two N_2 physisorption isotherms are similar (Figure 1b). The micropore volume of Z_{Si} and Z_{Al} are close to each other (Table 1). While the occurrence of narrow hysteresis loop at a relative pressure of 0.5 indicates the presence of mesopores in both samples, a similar mesopore volume was measured for both Z_{Si} and Z_{Al} (Table 1). The acidity of both Z_{Si} and Z_{Al} zeolites was measured by FT-IR using pyridine as a

probe molecule. The total acidity of Z_{Al} and Z_{Si} zeolite samples is similar, while the Z_{Al} zeolite has a slightly lower amount of Brønsted acid and a higher amount of Lewis acid than Z_{Si} (Figure 1c and Table 1). The ^{27}Al NMR spectra (Figure 1d) exhibit both Z_{Si} and Z_{Al} possessing sole tetra-coordinated framework Al species which is in good consistency with the acidity and elemental analysis. Similarly, the bulk Si/Al ratio of samples Z_{Si} and Z_{Al} determined by XRF is 18.0 and 20.3, respectively (Table 1).

Table 1. The porosity data, bulk and surface Si/Al ratios, and the acidity properties determined by chemisorption of pyridine for Z_{Si} and Z_{Al} zeolite samples.

Sample	S_{BET}[a]	V_{micro}[b]	V_{meso}[c]	Si/Al[d]	Si/Al[e]	B_{Py}[f] (μmol/g)	L_{Py}[f] (μmol/g)
Z_{Si}	412	0.15	0.06	18.0	11.9	389	80
Z_{Al}	408	0.16	0.06	20.3	14.8	353	121

[a] Specific surface area calculated by the BET method. [b] Micropore volume calculated with the t-plot method. [c] Mesopore volume ($V_{meso} = V_{total} - V_{mic).}$ [d] Si/Al measured by XRF. [e] Si/Al determined by XPS. [f] The Brønsted (B_{Py}) and Lewis (L_{Py}) acidity determined by pyridine adsorption by IR.

3.2 Differences between Z_{Al} and Z_{Si} zeolite samples

3.2.1 Macroscopic properties

While there are several similarities between samples Z_{Al} and Z_{Si}, the alternation of the mixing order of Al and Si sources changes substantially the morphology of the zeolite crystals. The Z_{Al} sample is shown as isolated zeolite crystals with a homogeneous particle size of ca. 5~7 μm covered with faceted layers (see SEM

images in SI, Figure S2). In contrast, the Z_{Si} sample contains zeolite crystals with a broader particle size distribution and diversified appearance (Figure S3). There are both isolated and aggregated zeolite crystals in this sample (Figure S3a). The multi-faceted zeolite crystals with a round morphology can also be seen in this sample (Figure S3b, c). In addition, particles with smooth surface and coffin-shaped morphology are presented (Figure S3d). The synthesis of the Z_{Si} was repeated 3 times and the results were reproducible. From the second and third synthesis batches (samples Z_{Si}-B2 and Z_{Si}-B3, respectively), similar aggregated crystals with coffin shape, and broad size distribution were identified (Figure S4a and S5). Therefore, the difference in crystals morphology and size is originated from the sequence of chemical addition, either Si or Al added first.

The ^{29}Si MAS NMR spectra of the two samples contain three peaks at -106 ppm, -112 ppm and -115 ppm (Figure S6). From the deconvolution of the spectra, the Si/Al ratio of 25 and 14 for samples Z_{Al} and $Z_{Si,}$ respectively was determined. The difference in the elemental analysis result and the results from the deconvoluted ^{29}Si NMR spectra suggests the diverse internal structure for the Z_{Si} and the Z_{Al}. The FTIR spectra (Figure S7) show the same type of hydroxyl groups for both Z_{Al} and Z_{Si} zeolite samples, including the hydrogen-bonded hydroxyl nests (3500 cm^{-1}), the hydroxyl associated with framework (3610 cm^{-1}) and extra-framework (3780 cm^{-1} and 3670 cm^{-1}) aluminum species (AlOH), the internal (3715 cm^{-1}) and external (3740 cm^{-1}) silanols (SiOH) [55]. The Z_{Al} zeolite contains a higher amount of external silanols

and hydroxyls associated with extra-framework aluminum species. On the other hand, the Z_{Si} zeolite sample contains a higher amount of hydroxyl nests.

The Si/Al ratios calculated based on the ^{29}Si MAS NMR spectra (25 and 14 for samples Z_{Al} and Z_{Si}, respectively) differ from the ones determined by XRF (20.3 and 18.0 for samples Z_{Al} and Z_{Si}, respectively; Table 1). This difference can be explained by considering both the ^{27}Al MAS NMR spectra (Figure 1d) and FTIR analysis (Figure S8) for as-synthesized and H^+-form zeolite samples, respectively. Despite the sole presence of tetra-coordinated Al species in the as-synthesized samples (Figure 1d), negligible amount of the extra-framework Al was also observed for the H^+-form zeolite samples in both FTIR spectra (Figure S7) and ^{27}Al MAS NMR spectra (Figure S8). These extra-framework Al species are probably produced during the calcination and ion exchange procedures applied to the samples and they are probably related to zeolite framework defects. The structural defects can be detected by ^{29}Si NMR. A diversified chemical composition determined by ^{29}Si NMR compared with the XFR analysis was found [12]. The similar Al-rich crystal surface was confirmed by combining the XPS and XRF analysis[56, 57]. The results suggested preferential nucleation of the Si-rich gel species [44]. Additionally, the zeolite crystals in sample Z_{Si} exhibited a lower surface Si/Al ratio (11.9) compared with that of sample Z_{Al} (14.8). Consistently, the FTIR spectra recorded under adsorption of collidine (Figure S9) merely interact with the Brønsted acid sites on crystals outer surface revealed the higher amount of crystal surface acidity of sample Z_{Si} (9 $\mu mol \cdot g^{-1}$) in comparison to

sample Z_{Al} (4 μmol·g^{-1}). These results further highlight the different crystal architecture of the two zeolite samples.

3.2.2 Dissolution behavior

The similarities and differences of samples Z_{Al} and Z_{Si} were measured macroscopically. Yet the structural similarities and differences beneath the outer surface of zeolite samples have been little explored. Here we study the dissolution behavior of both Z_{Al} and Z_{Si} zeolites in fluoride medium aiming to obtain information about the internal architecture of the zeolite crystals.

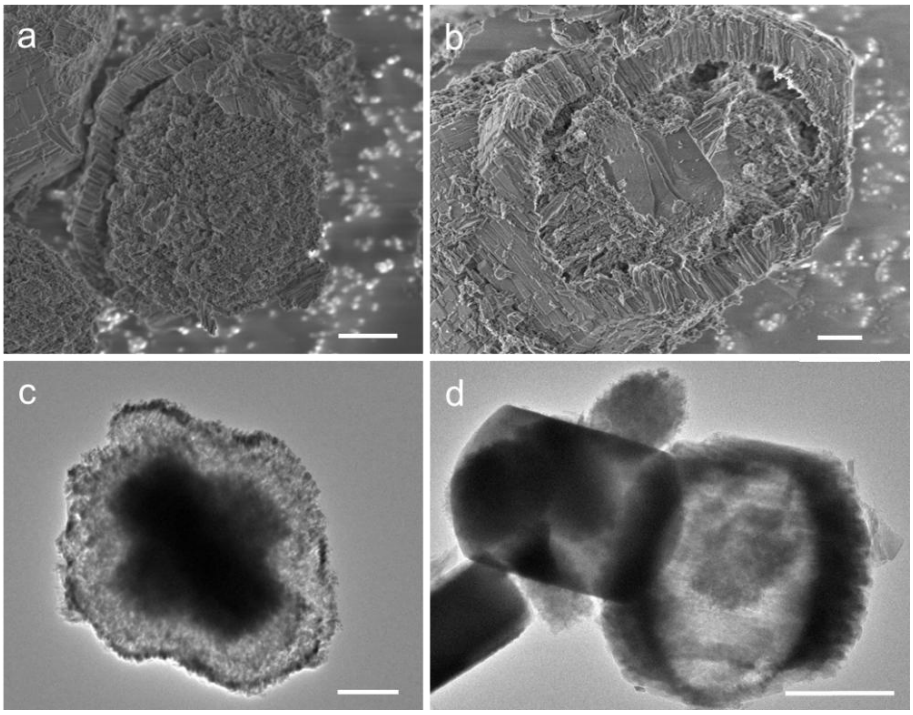

Figure 2. Zeolite samples characterized by SEM: Z_{Al}-AF (a) and Z_{Si}-AF (b) and by TEM: Z_{Al}-AF (c) and Z_{Si}-AF (d). Scale bar = 1μm.

Both as synthesized Z_{Al} and Z_{Si} zeolites prior to calcination were treated by concentrated NH_4F following the procedure described by our group [44]. After the

fluoride treatment using the same experimental conditions, both samples, Z_{Al}-AF and Z_{Si}-AF, showed a weight loss of ca. 50 wt.% and an increased Si/Al ratio in comparison to the parent samples (Z_{Al} and Z_{Si}). The Si/Al ratio of 23.5 for the Z_{Al}-AF and 31.5 for the Z_{Si}-AF was measured. The ^{27}Al NMR spectra verified the sole presence of tetra-coordinated framework Al species in both samples Z_{Si}-AF and Z_{Al}-AF (Figure S10), showing that the extra-framework Al species are not formed during the treatment. The Z_{Al}-AF zeolite sample contains crystals with an egg-like structure (Figures 2a, b) including the innermost and Si-rich core (egg yolk), the middle and defect-rich zone (egg white), and the outermost and uniform-oriented shell (egg shell) [44]. Similarly, the Z_{Si}-AF zeolite sample contains crystals with a multilayer structure. However, the Z_{Si}-AF crystals contain fewer "egg-white" and more "egg-shell" parts than the Z_{Al}-AF crystals (Figures 2a, b). The Z_{Al}-AF zeolite crystals appear as a nano-sponge. The innermost and condensed core of the Z_{Al}-AF zeolite sample is hidden inside the nano-sponge. The presence of a dense core is only observed by TEM (Figure 2c). On the other hand, a similarly condensed core in the Z_{Si}-AF zeolite sample is observed directly by SEM (Figures 2b and S11). The distinct presence of the outmost shell and the bare core part in the Z_{Si}-AF zeolite sample is also confirmed by TEM (Figures 2d and S12). The reproduced zeolite samples of Z_{Si} (Z_{Si}-B2 and Z_{Si}-B3) were also subjected to NH_4F treatment; the results demonstrated the distinctive dissolution behavior and internal architecture of the Z_{Si} (Figures S4b-d and S13).

The inner structure of zeolite crystals was further characterized by SEM combined with EDX spectroscopy. The cross-sections of zeolite crystals are shown in Figure 3. As reported previously, the Z_{Al} zeolite crystals show a single whitish circle under the electron beam irradiation [44]. Interestingly, there are multiple layers of such circular feature in the case of Z_{Si} zeolite sample. The reason for the existence of such whitish zones remains unknown. The preferential etching of Na-rich and/or defect-rich zones [44] transforms the dense middle layer of Z_{Al} zeolite crystals into a more porous layer. On the other hand, the "egg white" part almost disappears in the case of the Z_{Si}-AF zeolite (Figure 3d). The observed dissolution behavior implies that various defect-zoning in the two zeolite crystals is present, i.e., the defect sites in the Z_{Si} crystals are more enriched in the egg-white regions. These findings are consistent with the SEM and TEM results presented in Figure 2.

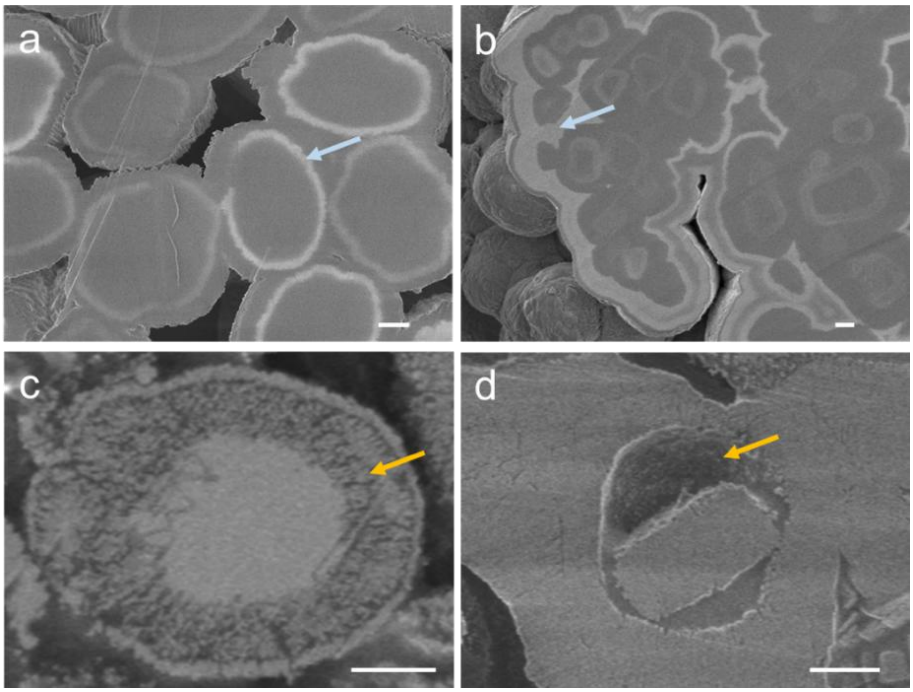

Figure 3. Cross-section SEM images of parent zeolite samples Z_{Al} (a) and Z_{Si} (b), and NH_4F treated zeolite samples Z_{Al}-AF (c) and Z_{Si}-AF (d). Scale bars = 1 μm. The preferentially dissolved regions are marked in the SEM images with arrows.

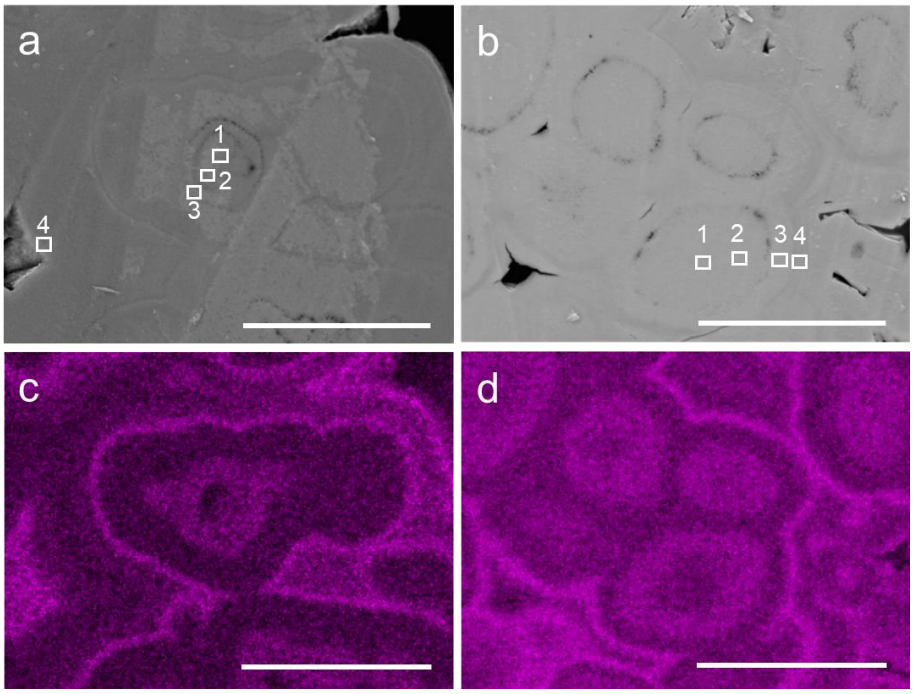

Figure 4. SEM images and cross-section SEM-EDX mapping of samples Z_{Si} (a and c) and Z_{Al} (b and d). Scale bar = 5 μm. (the figures for Z_{Al} (b and d) are quoted from our previous research paper [44]).

The spatial element distribution in the zeolite cross-section images was analyzed by SEM-EDS. The SEM-EDS mapping results (Figures 4 and Table 2) show a similar Al-zoning in both Z_{Si} and Z_{Al} zeolite samples. As the Z_{Si} sample is heavily aggregated, it is difficult to distinguish one crystal from other. The conclusion we may draw is that the Al distribution in Z_{Si} zeolite crystals is not homogeneous. After NH_4F etching of sample Z_{Si}, the periphery of the crystals becomes more distinct and clearer (Figure S14). In comparison to the parent sample (Z_{Si}), the Si/Al of the Z_{Si}-AF

zeolite is increased as measured by point analysis (Figure S14 and Table S1). This result suggests the preferential dissolution of Al-rich zones during the NH_4F treatment. This result is in line with the XRF analysis showing that the NH_4F etching of the Z_{Si} zeolite results in a sharp increase of the bulk Si/Al ratio from 18.0 to 31.5. Noticeably, the increase of the Si/Al ratio for the Z_{Si}-AF zeolite sample is much higher than that of Z_{Al}. The bulk Si/Al increased from 20.3 to 23.5 after NH_4F etching under the same treatment conditions as applied for sample Z_{Al} [44]. This observation points out the distinct difference in the Si and Al distributions of samples Z_{Si} and Z_{Al}. More specifically, the dissolved parts in the Z_{Si} zeolite should have a much higher amount of Al than in the Z_{Al} zeolite, thus pointing to a more biased element (Si, Al, Na^+, and TPA^+) distribution in the Z_{Si} zeolite sample.

Initial gel precursor for sample Z_{Si} were prepared and subjected to extended aging time (12 and 60 h) prior hydrothermal synthesis to rule out the effect of aging treatment on crystals features. In comparison with the original sample Z_{Si}, the new one obtained after aging of the precursor gel for 12 h (Z_{Si}'-12A) shows similar crystal morphology (Figure S3 e-f). Even after aging for 60 h of the precursor gel, the final crystals (Z_{Si}'-60A) still retain the same shape (Figure S3 g-h). The Z_{Si}'-12A shows similar chemical composition (Si/Al = 18.7, Table S2) as the original sample Z_{Si}, and still Al-rich crystal surface despite of the slightly higher Si/Al (Si/Al = 16.0, Table S2). The zeolite samples (Z_{Si}'-12A and Z_{Si}'-12A) obtained after extended aging of the gels exhibit similar regioselective dissolution behavior in NH_4F solution (Figures S15-S17). The SEM-EDX analysis confirms the siliceous innermost core of sample

$Z_{Si}^{'}$-12A-AF (Figure S15f). In addition, the measured Si/Al of the $Z_{Si}^{'}$-12A-AF sample (Si/Al = 39.2, Table S2) further indicates that the different aging duration did not cause changes on the inner architecture of the final product.

Table 2. Element composition of Z_{Si} and Z_{Al} zeolite samples determined by EDX at selected zones presented in Figures 4a and b. (the data for Z_{Al} is quoted from our previous research paper [44]).

Zones in sample Z_{Si}	Si [a]	Al [a]	Si/Al [b]	Zones in sample Z_{Al}	Si [a]	Al [a]	Si/Al [b]
1	28.42	0.99	28.7	1	30.31	0.84	34.8
2	28.94	1.14	25.4	2	29.33	1.62	17.5
3	27.25	1.60	17.0	3	28.26	2.19	12.4
4	26.00	2.92	8.9	4	27.92	1.47	18.3

a: the relative atomic content of elements (%) measured by EDX; b: the atomic Si/Al ratio calculated based on the EDX results.

3.2.3 Effect of mixing order of Si and Al on the evolution of Z_{Al} and Z_{Si} zeolite samples

As noted above, the exchange of the mixing order of chemicals for the preparation of samples Z_{Al} and Z_{Si} resulted in multi-layer structures distinguished by Al-zoning and defect-zoning in the inner part of the zeolite crystals. The two Z_{Al} and Z_{Si} zeolites have different Si/Al ratios and different solubility in NH_4F solutions as shown in Figures 2-4 and Table 2. As stated by Corma, all the intelligence is already contained in the starting reagents that undergo mysterious self-assembly under auxiliary heating in a closed environment [58]. Thus, the way how the TO_4 tetrahedra (T: Si^{4+}, Al^{3+}, etc.) are mixed and organized may significantly impact the macroscopic properties of the final outcomes. In the following section, the procedures for the preparation of the

precursors and their continuous evolution during the hydrothermal treatment will be disclosed (Scheme 1).

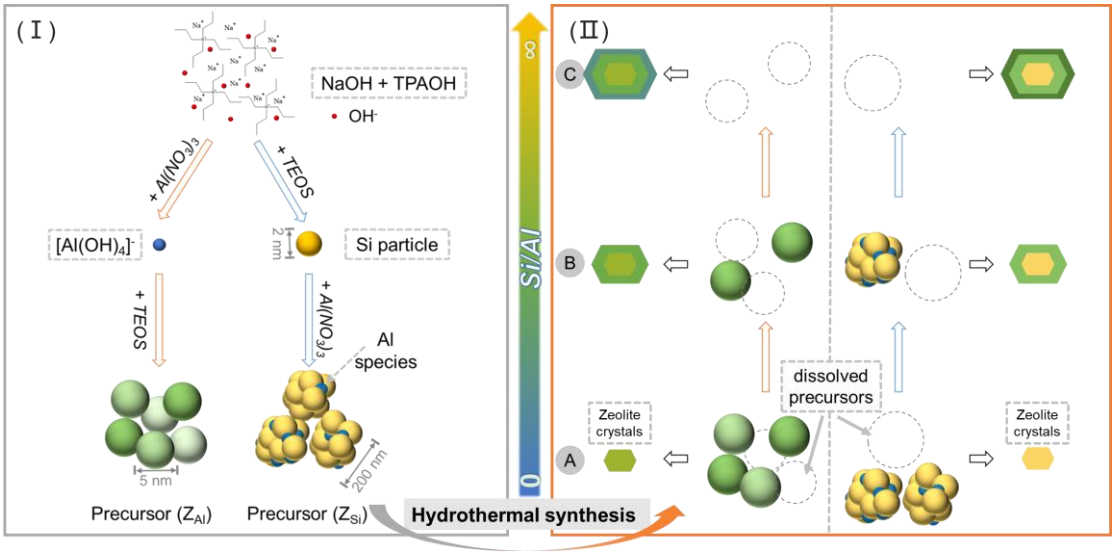

Scheme 1. Schematic presentation of (Ⅰ) the preparation of precursor mixtures for the synthesis of Z_{Al} and Z_{Si} zeolites and (Ⅱ) the evolution process of the precursors resulting in fully crystalline zeolites (A: the initial nucleation stage; B: the fast aggregate growth process; C: the layer-by-layer growth).

For the synthesis of the Z_{Al} zeolite (Scheme 1(Ⅰ)), the aluminum nitrate was firstly dissolved in NaOH and TPAOH solution resulting in an Al-containing solution with a pH of 12.89. The Al species in that solution exists primarily as monomeric ions ($Al(OH)_4^-$) or simple dehydration products such as AlO_2^- [59]. Then the Si source (TEOS) was added and gradually hydrolyzed in the homogeneous alkaline solution. The released Si species interact intimately with the Al species through the hydrolysis and dynamic condensation process. The generated aluminosilicate species are mainly involve with the TPA^+ cations due to the negatively charged surface [60], while the Na^+ cations mainly exist in the solution [61]. Finally, the obtained precursor mixture appears

as a transparent sol (Figure 5a) contain low-weight aluminosilicate homogeneous particles with a size of 5 nm at a pH of 11.09 (Figure 5b) [62].

The preparation of Z_{Si} precursor mixture started by hydrolysis of the silica source (TEOS) in the presence of NaOH and TPAOH (Scheme 1(Ⅰ)). The spontaneous condensation of Si species leads to the formation of colloidal silica particles with an average size of 2-3 nm at a pH of 11.60 (Figure 5b). Then the same amount of the Al was dissolved in water and added drop-wise into the Si-containing mixture. This resulted in a milky gel (Figure 5a) containing particles with a size of ca. 200 nm (Figure 5b); the addition of polyvalent Al^{3+} cations may cause coagulation of the particles (Scheme 1(Ⅰ)). The refractive index and density of the precipitate are both higher than in the surrounding liquid, and the precipitate is visible (Figure 5a) [61]. The final pH of the Z_{Si} precursor mixture was 11.07. Importantly, both precursor mixtures have the same gel composition and similar pH.

The silicon environment in both precursor mixtures was probed by ^{29}Si MAS NMR-CP spectroscopy (Figure 5c). Same Si species were detected in the two precursor mixtures, including the Q_4 (Si(4Si)) species occurring at ca. -110 ppm and Q_3 (Si(3Si)) species at ca. -96 ppm. In the Z_{Al} precursor mixture, the hydrolyzed Si species instantly interact with the Al in the solution, resulting in a dispersed Al species (Scheme 1) in the final precursor gel (lower amount of Q_4 species). In contrast, during the hydrolysis of TEOS, Si gel particles preferentially are generated with enriched Q_4 (Si(4Si)) species. Along with the addition of Al source, the synthesis mixture still contains higher amount of Q_4 species (Si(4Si)) [61] (Scheme 1).

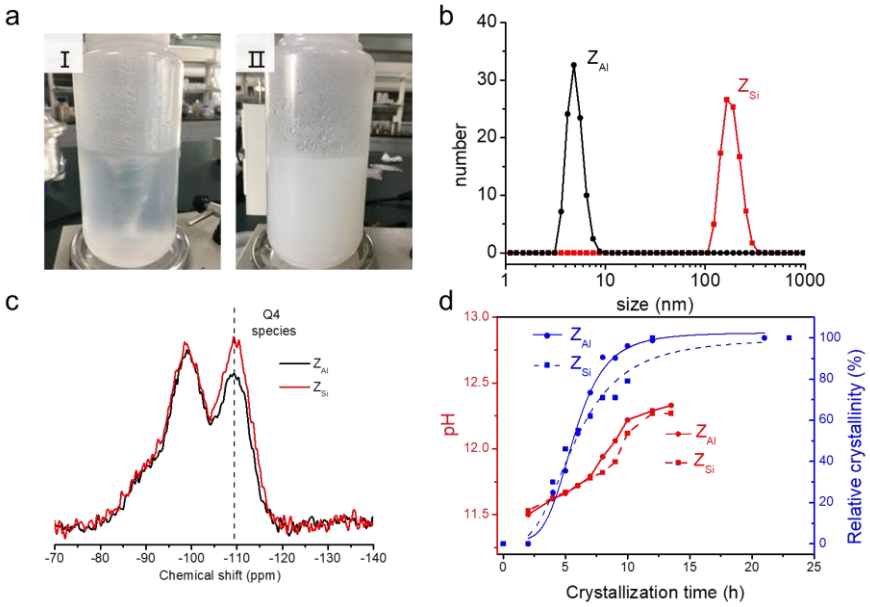

Figure 5. (a) Photos of the precursor mixtures used for the synthesis of Z_{Al} (I) and Z_{Si} (II) zeolites samples, (b) particle size distribution of precursor mixtures Z_{Al} and Z_{Si} measured by dynamic light scattering (DLS), (c) ^{29}Si MAS NMR-CP spectra of the freeze-dried precursor mixtures Z_{Al} and Z_{Si}, and (d) evolution of the crystallinity (blue) and pH (red) in precursor mixtures Z_{Al} and Z_{Si} during the hydrothermal treatment (the curves for Z_{Al} in b and d are quoted from our the previous research paper [44]).

The precursor mixtures were transferred into Teflon-lined autoclaves and subjected to heating in a convection oven at 443 K for up to 24 h (Scheme 1(Ⅱ)). Intermediate samples, Z_{Al}-x and Z_{Si}-x were collected during the synthesis and subjected to characterization. After 2 h heating, the first intermediate samples, Z_{Al}-2 and Z_{Si}-2 were amorphous (Figure S18). Both samples contained ultra-small nanoparticles (Figures S19 and S20), however the Z_{Si}-2 sample contains particles with a higher degree of aggregation in comparison to the Z_{Al}-2 sample. This microscopical

observation corresponds to the particle size distribution determined by DLS (Figure 5b). After 4 h of heating, the intermediate samples, Z_{Si}-4 and Z_{Al}-4 contained already the Bragg peaks associated with the appearance of the MFI phase (Figure S18), with the former being more crystalline than the latter. The higher crystallinity of Z_{Si}-4 was further supported by the higher micropore volume (Table S3), which is attributed to the physisorption of Ar molecules in the micropores of the zeolite (Figures S21 and S22). In addition, the presence of round-boat-shaped crystallites with a flat surface and a deficiency in Al content in the case of Z_{Si}-4 sample were observed (Figures S23a, b and S24). The ubiquitous presence of these regular-shaped crystallites in the intermediate samples (Figure S23), fully crystalline (Figure S3d) and the NH_4F treated samples (Figures 2, 3, S11 and S12) in the case of Z_{Si} zeolite is clearly observed. In contrast, the sample Z_{Al}-4 contained irregular-shaped aggregates without regular-shaped crystallites (Figures S25a, b).

The difference in the early stage of crystallization is evidently observed for samples Z_{Si} and Z_{Al}. While in both cases the Si-rich parts in the sol or hydrogel undergo the structure reorganization first (Scheme 1(II)), as the surface adsorption of aluminium significantly retards the dissolution of silica [62], the nucleation environment in the case of Z_{Si} should be richer in Si, which is in turn more favorable for the occurrence of the first crystallites (Figures 5d and S18). This leads to a more heterogeneous distribution of Si and Al in the Z_{Si} precursor system (Scheme 1(II)). Apparently, the mixing order of Si and Al changes substantially the hydrolyzation rate and condensation of Si and Al species which has a direct impact on their evolution and subsequent nucleation and

growth. In general, the Si-rich zone is more favorable for nucleation in the precursor system thanks to its higher solubility and attraction to the organic template. On the other hand, since the bulk composition of the two precursors are essentially the same, the preferential consumption of Si source for nucleation will leave behind a relatively Al-richer aluminosilicate sol/gel (Scheme 1(II)), which is the nutrient source for the following crystal growth.

After 4 h of hydrothermal treatment, both samples become partially crystalline. The sigmoidal crystallization curves describing the synthesis of both samples are depicted in Figure 5d. With the sharp increase of the sample crystallinity, an increase of surface roughness of the previously smooth-surface crystallites in the case of Z_{Si}-6 was observed (Figures S23c and d), where the profile of the round-boat-shaped crystallites was still distinguishable. On the other side, the Z_{Al}-6 sample contained irregular-shaped crystals (Figures S25c and d). The crystallinity of the samples increased accompanied by a slightly delayed steep of increased pH of the solution (Figure 5d). After the first stage of crystallization which corresponds to the occurrence of the zeolite core (egg-yolk) nucleated in a Si-rich environment, the second stage characterized by the fast amorphous-to-crystalline transformation is proceeding. The second stage is characterized by the fast and oriented attachment of aluminosilicate particles to the zeolite core (Figures 5d, S23 and S25). This results in the formation of the middle layers enriched in defects (Figures 2 and 3). The continuous condensation of silicate species and the growth of zeolite crystals lead to the release of the OH^- into the solution [63, 64]. The pH of the synthesis media increases

(Figure 5d), which favors the dissolution and/or reorganization of the Al-rich aluminosilicate gels (Scheme 1(Ⅱ)). This results in the formation of the Si-rich core and the gradual decrease of the Si/Al of the particles from the core to the rim (Figure 4 and Table 2).

After 12 h of heating, the zeolite crystals have similar morphology (Figures S23 and S25). The crystallinity of the samples changed negligibly (Figures 5d and S18) which is consistent with the slightly improved micropore volume (Figures S17, S22, and Table S3) and similar pH variation in the mixtures (Figure 5d). This last stage corresponds to the asymptotic phase of the sigmoidal growth, in which the curve approaches a plateau, and the crystal growth is dominated by a layer-by-layer mechanism that shaped the morphology of the zeolite crystals and leads to the densification of the aggregates.

While the general crystallization trend in the two synthesis systems is the same, one can notice that the two curves crossed at ca. 5 h of crystallization time, indicating a faster nucleation but a slower crystallization for sample Z_{Si} in comparison to sample Z_{Al}. This is consistent with the micropore volumes measured for these two samples (Table S3 and Figure S22). This change can be related with the different consumption of Si during the nucleation and early growth stage in sample Z_{Si}. This is reasonable if one considers the mass balance of the two synthesis systems. Namely, the two precursors have the same bulk composition, but the nucleation in the case of Z_{Si} consumes more Si than in the Z_{Al} (Scheme 1(Ⅱ)). Thus, the aluminosilicate precursor has higher Al content during the crystal growth stage in the case of $Z_{Si.}$ A higher pH is

required to hydrolyze the Al richer aluminosilicate gel, in order to provoke the transformation from amorphous-to-crystalline particles.

3.2.4 Catalytic behaviors of Z_{Al} and Z_{Si} zeolite samples in n-hexane cracking and ethylene dehydroaromatization reactions

a) n-hexane cracking reaction

The n-hexane cracking reaction was used to characterize the acidic properties of the zeolite samples. The turnover frequencies (TOF) per Brønsted acid sites of samples Z_{Si} and Z_{Al} in comparison to the parent Z_P sample are summarized in Table 3. The TOF of the parent Z_P sample is 314 h^{-1}, which is 2.6 to 3.5 times lower than for samples Z_{Si} and Z_{Al}, respectively. Additionally, the TOF for a series of commercial ZSM-5 catalysts free of EFAL species with Si/Al ratios ranging from 10 to 75 are presented in Figure S26.

Table 3. The turnover frequency (TOF) per Brønsted acid site of zeolite catalysts in n-hexane cracking reaction

Catalysts	Z_{Si}	Z_{Al}	Z_P (Reference)
TOF (h^{-1})	814	1092	314

The higher cracking activity of samples Z_{Si} and Z_{Al} in comparison to the parent Z_P zeolite is ascribed to the presence of EFAL through an exaltation of BAS strength [65-67]. Indeed, a combined MAS NMR with DFT study showed the interactions between the BAS and Lewis acid sites (LAS) leading to an increase of the acid site strength of the zeolite catalyst[68]. Moreover, the higher cracking activity of samples

Z_{Al} than Z_{Si} are attributed to the higher amount of EFAL species as shown by FTIR and ^{27}Al NMR spectroscopy (Figure s7 and S8).

b) Ethylene dehydroramatization reaction

EDA is a process involving the protonation of ethylene by BAS [69-71] and further reactions, the oligomerisation and protolytic cracking, proceeding via carbenium ions as intermediates. High temperature [69, 71-74] and low olefin partial pressure (P_{C2H4}) [72, 74-78] have been reported to constrain the oligomerisation reaction. For example, the ethylene conversion at 475 °C under atmospheric pressure using dilute ethylene (P_{C2H4} = 0.013 MPa) is only 2 % [75] over ZSM-5 catalyst (Si/Al = 103). On the other hand, over 83 % conversion over the same catalyst at 350 °C with a P_{C2H4} of 0.1 MPa was reported [76]. Since ethylene activation depends on the Brønsted acid site density, more specifically on the concentration of next-nearest neighbors of Al centers[72], the ethylene transformation can be used as a good descriptor of the textural properties of zeolites.

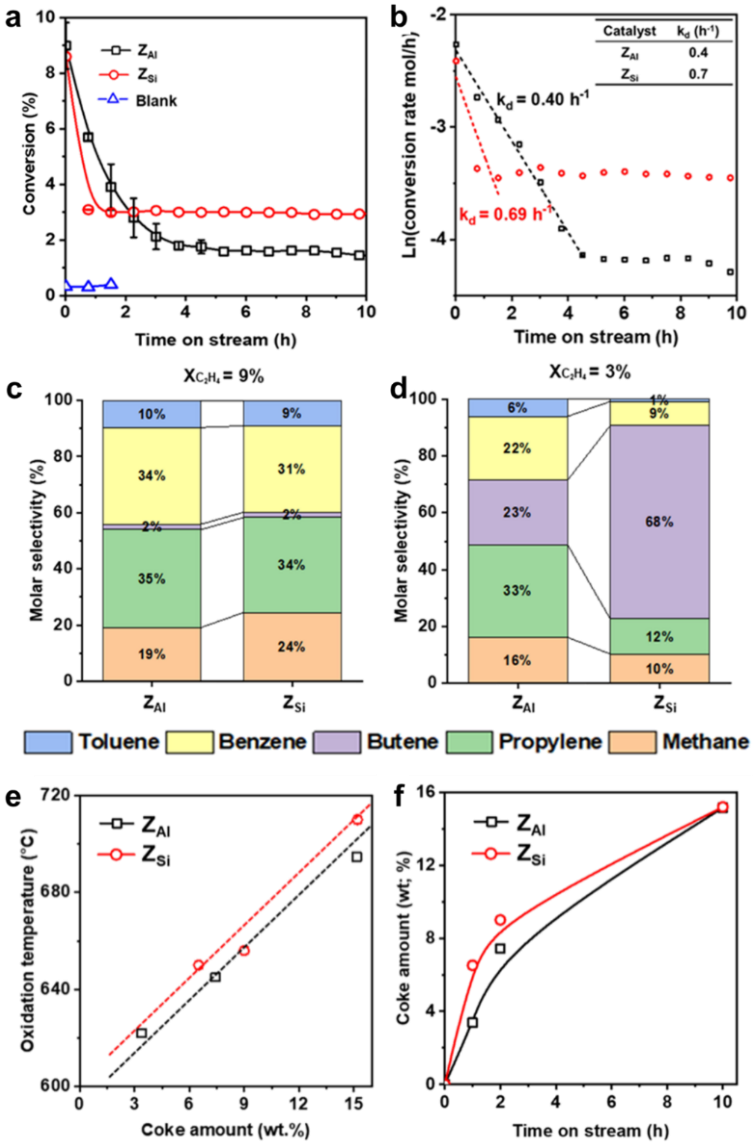

Figure 6. (a) Conversion of ethylene on Z_{Si} and Z_{Al} zeolite samples as a function of the time on stream, and (b) deactivation rates of Z_{Al} and Z_{Si} zeolite samples based on the assumption of an exponential function. *Inset* in (b): the deactivation constant (k_d). Molar selectivity of the formed products at iso-conversion, i.e. (c) initial time on stream and (d) the conversion of 3%. (e) Coke amount recovered as a function of the time on stream for Z_{Si} and Z_{Al} zeolite samples and (f) oxidation temperature of the coke as a function of its amount.

The ethylene conversion on the two samples as a function of the time on stream is depicted in Figure 6a. The reaction was carried out at a low contact time and therefore no induction period is reported [71]. The initial conversion is similar for both samples (~9%). The TOF (turnover frequency) computed from the concentration of BAS for the two zeolite catalysts (145 h^{-1} for Z_{Al} and 119 h^{-1} for Z_{Si}) is nearly the same and comparable to that reported in the open literature [69]. The catalysts started to deactivate and reached a plateau stage at 1 h and 4 h for samples Z_{Si} and Z_{Al}, respectively. Assuming an exponential function [79], the calculated deactivation constant is presented in Figure 6b. Noticeably, Z_{Si} showed an almost twice faster deactivation rate (0.7 h^{-1}) than the Z_{Al} (0.4 h^{-1}). After the quick deactivation period, the two zeolite catalysts reached a plateau stage. Specifically, the ethylene conversion over the Z_{Si} zeolite was stable with a conversion of ~ 3%, while only half for the Z_{Al} zeolite is measured. It is important to point out that the catalytic test in an empty reactor achieves only 0.5% of conversion, which indicates that there is no significant thermal dimerization/cracking reaction.

The molar selectivity of the products at the initial time on stream at 9% conversion (Figure 6c) and at 3% conversion (Figure 6d) are shown. The steady-state results for Z_{Si} are shown in Figures 6c and d. The initial molar selectivity was comparable (Figure 6c). Benzene and propylene were found in large proportions. However, at 3% ethylene conversion (the plateau stage of the Z_{Si}), the two zeolite catalysts demonstrated markedly different product selectivity (Figures 6c and 6d). Butene, which is scarce at the beginning of the reaction, increased dramatically to 68% using

the Z_{Si} zeolite catalyst, while in the case of Z_{Al}, the increase is only 23% (Figure 6d). Furthermore, at lower ethylene conversion, the two zeolite catalysts formed different proportions of methane to propylene (C1/C3). When compared to the initial stage of the reaction (Figure 6c), the Z_{Al} catalyst maintained nearly the same ratio of derived methane to propylene (Figure 6d), whereas the Z_{Si} catalyst produced nearly the same amount of methane and propylene (C1/C3 molar ratio is equal to 1, Figure 6d), much higher than its initial ratio. The difference in product selectivity is related to the higher cracking activity of samples Z_{Al} than Z_{Si}, as shown in the case of n-hexane cracking reaction (Figure S26).

The formation of coke on the two zeolite samples was investigated throughout the reaction lifetime. From the thermogravimetric analysis, the coke amount and oxidation temperatures were determined (Figure S27). The coke content plotted as a function of the time on stream is presented in Figure 6e. Both catalysts displayed the same amount of coke after 10 hours of reaction. However, a difference occurred at a lower reaction time on stream. Namely, the initial coking rate is faster for sample Z_{Si} (Z_{Si}: 45 mg g_{cat}^{-1} h^{-1}; Z_{Al}: 35 mg g_{cat}^{-1} h^{-1}), explaining its faster deactivation rate (Figures 6a and b). As revealed by the FTIR analysis (Figure S7), a higher amount of hydroxyl nests was found in sample Z_{Si} that may act as a coke trap and lead to a faster coke deposition. In addition, all peaks in the differential thermal analysis (Figure S27) shifted to higher temperatures with increasing the coke amount in the zeolite samples (Figures 6f and S27). This is most likely related to a decrease of coke accessibility as the content increases. The Z_{Si} shows a considerably higher coke combustion temperature than Z_{Al}

on a comparative basis (Figure 6f). The microscopy study (Figures S2 and S3) revealed a wider particle size distribution of sample Z_{Si} which would hinder the coke combustion. In addition, a higher amount of silanol species was found in sample Z_{Al} which is considered to promote coke combustion. As a result, the Z_{Si} sample displayed a higher coke combustion temperature than sample Z_{Al}.

As can be seen from the results shown above, despite the fact that the two zeolite samples synthesized using the same precursor compositions have similar porosity and acid properties, they differ in the catalytic performance. The deactivation behavior and product selectivity clearly revealed a distinction between samples Z_{Si} and Z_{Al}. This study revealed the crystallization process and dissolution behavior of zeolites in two systems and the intimate synthesis-structure relationship was disclosed. Herein, the distinct catalytic behavior further underlines the significance of the crystal internal architecture, manifesting the significance of rationalized crystal engineering and more specifically, the control of Al sitting and distribution in the amorphous units formed prior the zeolite synthesis. It is worth mentioning that while most works focus on the impact of chemical sources on the spatial distribution of Al in zeolite frameworks, such as the Si source [80, 81], the Al source [82], and the structure-directing agents [36, 83-86], the present work details the impact of the chemical mixing order on the spatial distribution of Al in zeolites on meso- or macro-scales and the effect on their catalytic performance. This enriched the toolkit for the tailored design of zeolite crystals with required properties.

4. Conclusions

In summary, the alternation of the mixing order of Si and Al sources in the synthesis of zeolites did not impact the bulk composition, porosity, and acidity properties, however, it resulted in a substantial change of their inner architecture. The comprehensive study of the zeolite structures from both the top-down deconstruction of the as-synthesized zeolite crystals using the chemically unbiased NH_4F etching and the bottom-up tracking of the crystallization history is disclosed. Compared with the synthesis of zeolite Z_{Al} by adding Al source first to the precursor mixture, the synthesis of zeolite Z_{Si} by adding Si source first resulted in a zeolite sample with a more diversified macroscopic morphology and more biased spatial distribution.

The different partitioning of Al is caused by the alternation of the chemicals' mixing order that changes substantially the hydrolyzation and condensation rates of Si and Al species, which has a direct impact on their evolution and subsequent nucleation and growth. The Si-rich zone is more favorable for nucleation in the precursor system due to its higher solubility and attraction to the organic template. As a result, the preferential consumption of Si source for nucleation leaves behind a relatively Al-richer aluminosilicate sol/gel for the following crystal growth when the bulk composition of the two precursors is essentially the same.

The two zeolite samples with different inner architectures showed obviously different catalytic activity, product selectivity and coking behavior in the EDA reaction, manifesting intimate synthesis-structure-performance relationship. Recently, an intriguing work was published by Rimer and his colleagues suggesting that it was possible to tailor the spatial distribution of Al and Si at the mesoscale by careful

selection of the synthesis parameters[36]. Further investigation of synthesis parameters including but not limited to chemical reagents of different reactivity and way of mixing for the tailored design of zeolite crystals at a single crystal level for targeted applications are highly valuable.

Author Contributions

The manuscript was written through contributions of all authors. All authors have given approval to the final version of the manuscript.

ASSOCIATED CONTENT

Supporting Information.

SEM and TEM images, SEM-EDX results, ^{29}Si MAS NMR spectra, XRD patterns, Ar (87K) sorption-desorption results and thermal analysis curves can be found in the supporting information.

Acknowledgements

Z.Q. acknowledges the support from NSFC 22178389; S.M. acknowledges the support from NSFC 21975285; Z.Q. and S.M. acknowledge the support from NSFC 21991090, NSFC21991091 and PetroChina (PRIKY21084, KYWX-21-021). S.M.: co-funded by the European Union (ERC, ZEOLIghT, 101054004). Views and opinions expressed are, however, those of the author(s) only and do not necessarily reflect those of the European Union or the European Research Council. Neither the European Union nor the granting authority can be held responsible for them. A.B. and

L.P. thank the European Union's Horizon 2020 research and innovation program for its funding under grant agreement No 814548. Views and opinions expressed are however those of the author(s) only and do not necessarily reflect those of the European Union. Neither the European Union nor the granting authority can be held responsible for them.

References

1. Verboekend D., Thomas K., Milina M., et al. Towards more efficient monodimensional zeolite catalysts: n-alkane hydro-isomerisation on hierarchical ZSM-22. Catalysis Science & Technology, **2011**, 1(8): 1331-1335.

2. Clatworthy E. B., Konnov S. V., Dubray F., et al. Emphasis on the Properties of Metal- Containing Zeolites Operating Outside the Comfort Zone of Current Heterogeneous Catalytic Reactions. Angewandte Chemie, **2020**, 132(44): 19582-19600.

3. Chen N. Y., Garwood W. E. Some catalytic properties of ZSM-5, a new shape-selective zeolite. J. Catal.;(United States), **1978**, 52(3).

4. Anderson J. R., Foger K., Mole T., et al. Reactions on ZSM-5-type zeolite catalysts. Journal of Catalysis, **1979**, 58(1): 114-130.

5. Kang M., Um M. H., Park J. Y. Synthesis and catalytic performance on methanol conversion of NiAPSO-34 crystals (I): effect of preparation factors on the gel formation. Journal of Molecular Catalysis A: Chemical, **1999**, 150(1-2):

195-203.

6. Li S., Li J., Dong M., et al. Strategies to control zeolite particle morphology. Chemical Society Reviews, **2019**, 48(3): 885-907.

7. Marques J. P., Gener I., Ayrault P., et al. Infrared spectroscopic study of the acid properties of dealuminated BEA zeolites. Microporous and mesoporous materials, **2003**, 60(1-3): 251-262.

8. Haw J. F. Zeolite acid strength and reaction mechanisms in catalysis. Physical Chemistry Chemical Physics, **2002**, 4(22): 5431-5441.

9. Pu X., Liu N., Shi L. Acid properties and catalysis of USY zeolite with different extra-framework aluminum concentration. Microporous and mesoporous materials, **2015**, 201: 17-23.

10. Verboekend D., Pérez-Ramírez J. Design of hierarchical zeolite catalysts by desilication. Catalysis Science & Technology, **2011**, 1(6): 879-890.

11. Qin Z., Cychosz K. A., Melinte G., et al. Opening the cages of faujasite-type zeolite. Journal of the American Chemical Society, **2017**, 139(48): 17273-17276.

12. Qin Z., Hafiz L., Shen Y., et al. Defect-engineered zeolite porosity and accessibility. Journal of Materials Chemistry A, **2020**, 8(7): 3621-3631.

13. De Jong K. P., Zečević J., Friedrich H., et al. Zeolite Y crystals with trimodal porosity as ideal hydrocracking catalysts. Angewandte Chemie, **2010**, 49(52): 10074-10078.

14. Breck D. W. Zeolite Molecular Sieves. New York, **1974**, 634.

15. Zhdanov S. P. Molecular Sieve Zeolites-I. Advances in Chemistry Series, **1971**, 101: 20.

16. Grand J., Awala H., Mintova S. Mechanism of zeolites crystal growth: new findings and open questions. CrystEngComm, **2016**, 18(5): 650-664.

17. Li R., Chawla A., Linares N., et al. Diverse physical states of amorphous precursors in zeolite synthesis. Industrial & Engineering Chemistry Research, **2018**, 57(25): 8460-8471.

18. Le T. T., Chawla A., Rimer J. D. Impact of acid site speciation and spatial gradients on zeolite catalysis. Journal of Catalysis, **2020**, 391: 56-68.

19. Knott B. C., Nimlos C. T., Robichaud D. J., et al. Consideration of the aluminum distribution in zeolites in theoretical and experimental catalysis research. ACS Catalysis, **2018**, 8(2): 770-784.

20. Davis M. E. In Catalysis by Crystalline Microporous Materials, Catalysis in Chemistry and Biology: Proceedings of the 24th International Solvay Conference on Chemistry, World Scientific: **2018**, p. 137.

21. Karwacki L., Kox M., Matthijs de Winter D. A., et al. Morphology-dependent zeolite intergrowth structures leading to distinct internal and outer-surface molecular diffusion barriers. Nature materials, **2009**, 8(12): 959-965.

22. Qin Z., Melinte G., Gilson J.-P., et al. The mosaic structure of zeolite crystals.

Angewandte Chemie, **2016**, 128(48): 15273-15276.

23. Davis M., Drews O., Ramanan H., et al. Mechanistic principles of nanoparticle evolution to zeolite crystals. Nature materials, **2006**, 5(5): 400-408.

24. Dědeček J., Tabor E., Sklenak S. Tuning the aluminum distribution in zeolites to increase their performance in acid- catalyzed reactions. ChemSusChem, **2019**, 12(3): 556-576.

25. Shamzhy M., Opanasenko M., Concepción P., et al. New trends in tailoring active sites in zeolite-based catalysts. Chemical Society Reviews, **2019**, 48(4): 1095-1149.

26. Ding K., Corma A., Maciá-Agulló J. A., et al. Constructing hierarchical porous zeolites via kinetic regulation. Journal of the American Chemical Society, **2015**, 137(35): 11238-11241.

27. Danilina N., Krumeich F., Castelanelli S. A., et al. Where are the active sites in zeolites? Origin of aluminum zoning in ZSM-5. The Journal of Physical Chemistry C, **2010**, 114(14): 6640-6645.

28. Van Loon J., Janssen K. P. F., Franklin T., et al. Rationalizing acid zeolite performance on the nanoscale by correlative fluorescence and electron microscopy. ACS catalysis, **2017**, 7(8): 5234-5242.

29. Von Ballmoos R., Meier W. M. Zoned aluminium distribution in synthetic zeolite ZSM-5. Nature, **1981**, 289(5800): 782-783.

30. Dessau R. M., Valyocsik E. W., Goeke N. H.. Aluminum zoning in ZSM-5 as revealed by selective silica removal. Zeolites, **1992**, 12(7): 776-779.

31. Ristanović Z., Hofmann J. P., Deka U., et al. Intergrowth Structure and Aluminium Zoning of a Zeolite ZSM- 5 Crystal as Resolved by Synchrotron- Based Micro X- Ray Diffraction Imaging. Angewandte Chemie, **2013**, 125(50): 13624-13628.

32. Aramburo L. R., Karwacki L., Cubillas P., et al. The porosity, acidity, and reactivity of dealuminated zeolite ZSM- 5 at the single particle level: the influence of the zeolite architecture. Chemistry–A European Journal, **2011**, 17(49): 13773-13781.

33. Le T. T., Shilpa K., Lee C., et al. Core-shell and egg-shell zeolite catalysts for enhanced hydrocarbon processing. Journal of Catalysis, **2022**, 405: 664-675.

34. Ghorbanpour A., Gumidyala A., Grabow L. C., et al. Epitaxial growth of ZSM-5@ Silicalite-1: A core–shell zeolite designed with passivated surface acidity. ACS nano, **2015**, 9(4): 4006-4016.

35. Wang Z., Liu Y., Jiang J., et al. Synthesis of ZSM-5 zeolite hollow spheres with a core/shell structure. Journal of Materials Chemistry, **2010**, 20(45): 10193-10199.

36. Le T. T., Qin W., Agarwal A., et al. Elemental zoning enhances mass transport in zeolite catalysts for methanol to hydrocarbons. Nature Catalysis, **2023**, 6(3): 254-265.

37. Schmidt J. E., Poplawsky J. D., Mazumder B., et al. Coke formation in a zeolite

crystal during the methanol- to- hydrocarbons reaction as studied with atom probe tomography. Angewandte Chemie, **2016**, 55(37): 11173-11177.

38. Stavitski E., Kox M. H. F., Weckhuysen B. M. Revealing shape selectivity and catalytic activity trends within the pores of H-ZSM-5 crystals by time-and space-resolved optical and fluorescence microspectroscopy. Chemistry–A European Journal, **2007**, 13(25): 7057-7065.

39. Mores D., Stavitski E., Verkleij S. P., et al. Core–shell H-ZSM-5/silicalite-1 composites: Brønsted acidity and catalyst deactivation at the individual particle level. Physical Chemistry Chemical Physics, **2011**, 13(35): 15985-15994.

40. Aramburo L. R., Ruiz-Martínez J., Hofmann J. P., et al. Imaging the effect of a hydrothermal treatment on the pore accessibility and acidity of large ZSM-5 zeolite crystals by selective staining. Catalysis Science & Technology, **2013**, 3(5): 1208-1214.

41. Attila Ö., King H. E., Meirer F., et al. 3D Raman Spectroscopy of Large Zeolite ZSM-5 Crystals. Chemistry–A European Journal, **2019**, 25(29): 7158-7167.

42. Kokotailo G. T., Lawton S. L., Olson D. H., et al. Structure of synthetic zeolite ZSM-5. Nature, **1978**, 272(5652): 437-438.

43. Bozhilov K. N., Le T. T., Qin Z., et al. Time-resolved dissolution elucidates the mechanism of zeolite MFI crystallization. Science Advances, **2021**, 7(25): eabg0454.

44. Shen Y., Qin Z., Asahina S., et al. The inner heterogeneity of ZSM-5 zeolite

crystals. Journal of Materials Chemistry A, **2021**, 9(7): 4203-4212.

45. Kerr G. T. Chemistry of crystalline aluminosilicates. IV. Factors affecting the formation of zeolites X and B. The Journal of Physical Chemistry, **1968**, 72(4): 1385-1386.

46. Round C. I., Hill S. J., Latham K., et al. The crystal morphology of zeolite A. The effects of the source of the reagents. Microporous materials, **1997**, 11(3-4): 213-225.

47. Hincapie B. O., Garces L. J., Zhang Q., et al. Synthesis of mordenite nanocrystals. Microporous and mesoporous materials, **2004**, 67(1): 19-26.

48. Nazari M., Moradi G., Behbahani R. M., et al. Preparation and evaluation of the modified nanoparticle SAPO-18 for catalytic conversion of methanol to light olefins. Catalysis Letters, **2015**, 145(10): 1893-1903.

49. Chen C. T., Iyoki K., Hu P., et al. Reaction kinetics regulated formation of short-range order in an amorphous matrix during zeolite crystallization. Journal of the American Chemical Society, **2021**, 143(29): 10986-10997.

50. Dedecek J., Balgová V., Pashkova V., et al. Synthesis of ZSM-5 zeolites with defined distribution of Al atoms in the framework and multinuclear MAS NMR analysis of the control of Al distribution. Chemistry of Materials, **2012**, 24(16): 3231-3239.

51. Bok T. O., Andriako E. P., Knyazeva E. E., et al. Effect of the crystallization

mechanism on zeolite BEA textural and acidic properties. CrystEngComm, **2022**, 24(17): 3199-3207.

52. Ahmed S., Mohamed Z., Abdillahi M. M., et al. Investigation of the rapid crystallization method for the synthesis of MFI-type zeolites and study of the physicochemical properties of the products. Zeolites, **1996**, 17(4): 373-380.

53. Chatelain T., Patarin J., Soulard M., et al. Synthesis and characterization of high-silica EMT and FAU zeolites prepared in the presence of crown-ethers with either ethylene glycol or 1, 3, 5-trioxane. Zeolites, **1995**, 15(2): 90-96.

54. Asano N., Asahina S., Lu J., et al. Advanced scanning electron microscopy techniques for structural characterization of zeolites. Inorganic Chemistry Frontiers, **2022**, 9(16): 4225-4231.

55. Trombetta M., Armaroli T., Alejandre A. G., et al. An FT-IR study of the internal and external surfaces of HZSM5 zeolite. Applied Catalysis A: General, **2000**, 192(1): 125-136.

56. Qin W., Zhou Y., Rimer J. D. Deleterious effects of non-framework Al species on the catalytic performance of ZSM-5 crystals synthesized at low temperature. Reaction Chemistry & Engineering, **2019**, 4(11): 1957-1968.

57. Zhang J., Ren L., Zhou A., et al. Tailored synthesis of ZSM-5 nanosheets with controllable b-axis thickness and aspect ratio: Strategy and growth mechanism. Chemistry of Materials, **2022**, 34(7): 3217-3226.

58. Corma A., Davis M. E. Issues in the Synthesis of Crystalline Molecular Sieves: Towards the Crystallization of Low Framework- Density Structures. ChemPhysChem, **2004**, 5(3): 304-313.

59. Barrer R. M. Hydrothermal chemistry of zeolites. Academic Press, **1982**.

60. Iler K R. The chemistry of silica. Solubility, polymerization, colloid and surface properties and biochemistry of silica, **1979**.

61. Itani L., Liu Y., Zhang W., et al. Investigation of the physicochemical changes preceding zeolite nucleation in a sodium-rich aluminosilicate gel. Journal of the American Chemical Society, **2009**, 131(29): 10127-10139.

62. Ivanova I. I., Kolyagin Y G, Kasyanov I A, et al. Time- Resolved In Situ MAS NMR Monitoring of the Nucleation and Growth of Zeolite BEA Catalysts under Hydrothermal Conditions. Angewandte Chemie, **2017**, 129(48): 15546-15549.

63. Zones S. I., Jayanthi K., Pascual J., et al. Energetics of the local environment of structure-directing agents influence zeolite synthesis. Chemistry of Materials, **2021**, 33(6): 2126-2138.

64. Navrotsky A. Calorimetric insights into the synthesis of templated materials. Current opinion in colloid & interface science, **2005**, 10(5-6): 195-202.

65. Mirodatos C., Barthomeuf D. Superacid sites in zeolites. Journal of the Chemical Society, Chemical Communications, **1981**, (2): 39-40.

66. Niwa M., Sota S., Katada N. Strong Brønsted acid site in HZSM-5 created by

mild steaming. Catalysis Today, **2012**, 185(1): 17-24.

67. Haag W. O., Dessau R. M., Lago R. M. Kinetics and mechanism of paraffin cracking with zeolite catalysts[M]//Studies in Surface Science and Catalysis. Elsevier, **1991**, 60: 255-265.

68. Li S., Zheng A., Su Y., et al. Brønsted/Lewis acid synergy in dealuminated HY zeolite: a combined solid-state NMR and theoretical calculation study. Journal of the American Chemical Society, **2007**, 129(36): 11161-11171.

69. Beuque A., Barreau M., Berrier E., et al. Transformation of dilute ethylene at high temperature on micro-and nano-sized H-ZSM-5 zeolites Catalysts. **2021**, 11(2): 282.

70. Bessell S., Seddon D. Conversion of ethene and propene to higher hydrocarbons over ZSM-5. J. Catal.;(United States), **1987**, 105(1).

71. Vollmer I., Abou-Hamad E., Gascon J., et al. Aromatization of ethylene–main intermediate for MDA? ChemCatChem, **2020**, 12(2): 544-549.

72. Bonnin A., Comparot J. D., Pouilloux Y., et al. Mechanisms of aromatization of dilute ethylene on HZSM-5 and on Zn/HZSM-5 catalysts. Applied Catalysis A: General, **2021**, 611: 117974.

73. Uslamin E. A., Saito H., Kosinov N., et al. Aromatization of ethylene over zeolite-based catalysts. Catalysis Science & Technology, **2020**, 10(9): 2774-2785.

74. Dufresne L. A., Le Van Mao R. Hydrogen back-spillover effects in the aromatization of ethylene on hybrid ZSM-5 catalysts. Catalysis Letters, **1994**, 25: 371-383.

75. Gao J., Wei C., Dong M., et al. Evolution of Zn Species on Zn/HZSM-5 Catalyst under H_2 Pretreated and its Effect on Ethylene Aromatization. ChemCatChem, **2019**, 11(16): 3892-3902.

76. Ying L., Zhu J., Cheng Y., et al. Kinetic modeling of C2–C7 olefins interconversion over ZSM-5 catalyst. Journal of Industrial and Engineering Chemistry, **2016**, 33: 80-90.

77. Lukyanov D. B. Development of kinetic models for reactions of light hydrocarbons over ZSM-5 catalysts. experimental studies and kinetic modelling of ethene transformation and deactivation of HZSM-5 catalyst[M]//Studies in Surface Science and Catalysis. Elsevier, **1999**, 122: 299-306.

78. Qiu P., Lunsford J. H., Rosynek M. P. Characterization of Ga/ZSM-5 for the catalytic aromatization of dilute ethylene streams. Catalysis Letters, **1998**, 52: 37-42.

79. Levenspiel O. Experimental search for a simple rate equation to describe deactivating porous catalyst particles. Journal of Catalysis, **1972**, 25(2): 265-272.

80. Liang T., Chen J., Qin Z., et al. Conversion of methanol to olefins over H-ZSM-5 zeolite: reaction pathway is related to the framework aluminum siting. ACS

Catalysis, **2016**, 6(11): 7311-7325.

81. Pavlov V. S., Bruter D. V., Konnov S. V., et al. Effect of silica source on zeolite MFI crystallization in fluoride media and its physicochemical and catalytic properties. Microporous and Mesoporous Materials, **2022**, 341: 112088.

82. Sazama P., Dědeček J., Gabova V., et al. Effect of aluminium distribution in the framework of ZSM-5 on hydrocarbon transformation. Cracking of 1-butene. Journal of Catalysis, **2008**, 254(2): 180-189.

83. Yokoi T., Mochizuki H., Namba S., et al. Control of the Al distribution in the framework of ZSM-5 zeolite and its evaluation by solid-state NMR technique and catalytic properties. The Journal of Physical Chemistry C, **2015**, 119(27): 15303-15315.

84. Biligetu T., Wang Y., Nishitoba T., et al. Al distribution and catalytic performance of ZSM-5 zeolites synthesized with various alcohols. Journal of Catalysis, **2017**, 353: 1-10.

85. Di Iorio J. R., Gounder R.. Controlling the isolation and pairing of aluminum in chabazite zeolites using mixtures of organic and inorganic structure-directing agents. Chemistry of Materials, **2016**, 28(7): 2236-2247.

86. Muraoka K., Chaikittisilp W., Yanaba Y., et al. Directing Aluminum Atoms into Energetically Favorable Tetrahedral Sites in a Zeolite Framework by Using Organic Structure-Directing Agents. Angewandte Chemie, **2018**, 130(14):

3804-3808.